Modeling of Brillouin-assisted self-narrowed photonic oscillator including an optical phase-locked loop

Romain Agaisse, Gwennaël Danion, Marc Vallet, Pascal Besnard, Mehdi Alouini

Modeling of Brillouin-assisted self-narrowed photonic oscillator including an optical phase-locked loop

Romain Agaisse, Gwennaël Danion, Marc Vallet, Pascal Besnard and Mehdi Alouini

***Abstract*—We propose a theoretical description and experimental validation of a frequency self-stabilized photonic oscillator. This photonic oscillator which relies on a solid-state laser and a nonreciprocal Brillouin fiber resonator (BFR) arranged in an optical phase-locked loop (OPLL) was recently shown to provide very narrow linewidth in the Hz range. Special attention is given to end up with analytical expressions relying on coupled-mode formalism, of the BFR dynamics in which the non-resonant configuration for the pump has to be addressed. Furthermore, the transfer function of the full system is derived from the response of each component within the OPLL leading to two interleaved loops, relative to the phase and to the amplitude fluctuations of the optical field. An experimental setup including a solid-state Er:Yb laser is detailed and used to test the model predictions, both for phase noise level and response time. This model opens the way to the optimization of this new type of photonic oscillator which can be adapted to any kind of pump laser.**

***Index Terms*—Stimulated Brillouin scattering, optical frequency stabilization, fiber resonator**

I. Introduction

ULTRA narrow linewidth optical sources are useful or even compulsory in various applications. Among those applications, one can mention, e.g., time-frequency metrology [1] [2], microwave photonics [3] [4], coherent optical communications [5] [6], high-resolution spectroscopy, atomics clocks [7] and gravitational antennas [8]. In order to reach narrow linewidth, or equivalently low phase noise level, several solutions have been proposed. Diode-pumped solid-state bulk lasers [9], single-frequency fiber lasers [10], semiconductor lasers extended with external cavities [11] [12] or stabilized by means of self-injection locking [13], offer intrinsic linewidth that can reach a few tens of Hz and compact solutions for commercial applications (e.g. [14] [15]). To go further, linewidth narrowing setups can take advantage of external references provided by ultra-stable cavities [16] or molecular absorption lines [17]. These solutions can lead to sub-Hz intrinsic linewidths at the expense of more cumbersome setups. Another solution for good spectral properties is to use stimulated Brillouin scattering (SBS) in optical fiber [18]. Indeed, pumping an optical fiber above the SBS threshold generates a narrow gain, i.e. about 30 MHz-width, that offers a solution to use long active resonators. Accordingly the Stokes wave generated in such long fiber resonator exhibits a narrow linewidth [19] [20] [21]. However, the length of the resonator is usually limited to a few meters in order to ensure single frequency operation [22]. Indeed, for long resonators with associate free spectral range (FSR) smaller than the Brillouin gain width, several modes may oscillate, leading to natural mode hopping. To go beyond this limitation, we have recently proposed a new architecture based on a long non reciprocal Brillouin fiber resonator (BFR), i.e. a fiber loop longer than 100 m, coupled to an optical phase-locked loop (OPLL) [23]. The non-resonant configuration for the pump laser avoids the need of matching and locking the laser frequency to a BFR resonance [24], while the use of an OPLL provides a stable single-mode operation during hours. Indeed, as compared to microresonators [25], a very long BFR resonant for the pump would be rather difficult to inject due to its low FSR and to the hysteresis induced by the resonant pump power which gives rise to thermal and Brillouin refractive index change. In our architecture, the generated Stokes wave and the pump laser wave cannot be treated separately. They interact with each other leading to a spectral self-narrowing of the pump laser itself [26]. A theoretical description of such photonic oscillator is required in order to optimize the whole system and in particular its OPLL.

The aim of the present paper is thus to develop an analytical and predictive model of the Brillouin-assisted OPLL scheme. First, the BFR will be modeled using coupled-mode formalism, yielding a set of coupled equations for the three fields. Second, we represent the whole system behavior by means of a feedback loop. We will show that this loop, which acts as an OPLL, consists in two subloops, one for the phases and one for the amplitudes, interacting through amplitude-to-phase conversion processes. The paper is organized as follows. In Section 2, we describe the general principle of the method, the experimental setup, and the coupled mode model. Section 3 is devoted to the full analytical linearization of the various transfer functions associated to the OPLL. Section 4 compares the theoretical predictions with the experimental results obtained with our setup. Finally, the results are summarized and discussed in Section 5.

II. System description

A. Experimental arrangement

The general architecture of the complete system is depicted in Fig. 1. It includes a single mode laser whose linewidth will

Romain Agaisse, Marc Vallet, Pascal Besnard and Mehdi Alouini are with Univ Rennes, CNRS, Institut Foton - UMR 6082, F-35000 Rennes, France (e-mail: mehdi.alouini@univ-rennes1.fr).

Gwennaël Danion was with Univ Rennes, CNRS, Institut Foton - UMR 6082, F-35000 Rennes, France, (e-mail: gwennael.danion@gmail.com)

Manuscript received June 12, 2023; revised June 12, 2023.

narrow down as soon as the OPLL is closed. This laser, is slightly tunable with an external voltage. The useful output signal is a part of the laser beam. The remaining part is amplified using an erbium-doped fiber amplifier (OA) and acts as a pump for the nonreciprocal BFR which generates a backscattered Stokes wave. The Brillouin resonator is closed by an optical circulator enabling oscillation of the counter propagating Stokes wave while the forward propagating pump wave is annihilated after one round trip, making the BFR non resonant for the pump. At the output of the Brillouin fiber resonator, a fraction of the Stokes beam is mixed with the pump beam on a fast photodiode.

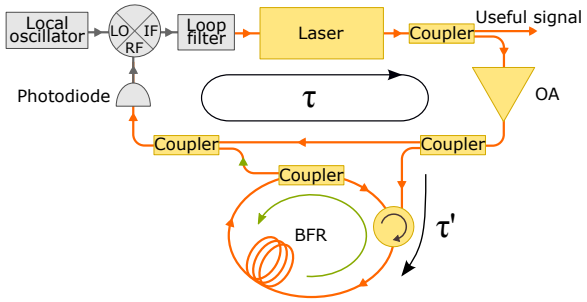

Fig. 1. Schematic of the photonic oscillator. Orange: optical fields. Grey: electrical signals. OA: optical amplifier. BFR: Brillouin fiber resonator not resonant for the pump. The beatnote between the Stokes and the pump is compared to a local oscillator to servo-control the laser frequency. τ, τ': delay times. (see text for details).

The beating electrical signal at the output of the photodiode is at a frequency corresponding to the Brillouin frequency shift with respect to the laser, here 11 GHz in our silica fiber. The wave mixing on the photodiode therefore results in a first frequency downshifting process from the optical domain to the radio frequency domain. The pump/Stokes beat note signal is then mixed with a local oscillator provided by a RF synthesizer set to the Brillouin frequency shift. This second down-conversion process from the radio frequency domain leads to a near DC signal. The resulting signal goes through an analog loop filter before being fed back to the laser which acts as a voltage controlled optical oscillator (VCOO). By freezing the frequency difference between the laser and the Stokes wave, this architecture forbids any mode hopping of the Stokes wave [23]. More importantly, the architecture will copy the inherent high spectral purity of the Stokes wave to that of the laser. Finally, the non-reciprocal nature of the Brillouin fiber resonator will naturally annihilate the oscillation of superior order Stokes waves. Such a system has been implemented and precisely described in Ref. [26]. We here briefly recall the main parts of our setup, while Table 1 lists the relevant parameters used in the numerical calculations.

We choose to use an Er,Yb solid-state laser as the free running linewidth of such laser is in the 10 kHz range which releases the constraint of realizing a large bandwidth PLL. Moreover, the PLZT ceramic inside the laser cavity does not limit the frequency tuning bandwidth (VCO effect) as compared to mechanical or thermal tuning.

The single-mode laser is a 6.8 mm-long diode-pumped solid-state Er:Yb laser. It emits 6 mW at λ = 1536 nm , when pumped with 400 mW at 980 nm. An intracavity PLZT ceramic allows us to tune the optical frequency ν_L, with a VCOO tuning rate $d\nu_L/dV$ equal to 20 MHz/V and a bandwidth of 2 MHz. We choose to use an Er,Yb solid-state laser because i) the free running linewidth of such laser is in the 10 kHz range which releases the constraint of realizing a large bandwidth PLL and ii) the PLZT ceramic does not limit the frequency tuning bandwidth as compared to mechanical or thermal tuning. 50% of the laser power is amplified by a homemade Erbium doped fiber amplifier (EDFA), resulting in a typical 110 mW pump power. 90% is injected into our BFR through the intracavity circulator. The BFR consists in a 110 m-long polarization-maintaining fiber coil molded in resin. The 10% port of the intracavity coupler provides the output Stokes power of around 10 mW. The beating signal is delivered by a fast InGaAsP fibered photodiode PD, whose bandwidth and transimpedance gain are respectively equal to 11 GHz and 440 V/W. The Stokes and pump power impinging on PD are set to 1 mW. The beatnote signal from the photodiode is then mixed with a 7 dBm local oscillator, provided by a RF synthesizer (Keysight Technologies N5183B) whose frequency is set at 10.998 GHz. Finally, the mixer output is sent into a proportional-integrator active filter.

B. Analytical description of the Brillouin resonator

As proposed by Loh et al. [27], a good starting point to model SBS resonators is to write the three wave mixing equations. However, our BFR has a peculiar architecture, since the pump field is not resonant with respect to the fiber resonator and the derivation of the field equations must thus take into account the non-reciprocal behavior of the resonator.

TABLE I
NUMERICAL VALUES OF THE PARAMETERS USED IN THE CALCULATIONS

n_0	refractive index of the BFR fiber	1.47
n_{loss}^P	Loss coefficient for the pump wave	$2,90.10^{-9}$
n_{loss}^S	Loss coefficient for the Stokes wave	$1,72.10^{-9}$
γ_e	Electrostrictive constant	$1,50$
S_{cf}	Mode field section inside BFR	$7,85.10^{-11} m^2$
Γ	Damping coefficient of the acoustic wave	$1,80.10^{-6}\ m^2/s$
v	Velocity of sound	$5968\ m/s$
ω_S	Stokes optical angular frequency	$1,23.10^{15}\ rad/s$
ω_P	Pump optical angular frequency	$1,23.10^{15}\ rad/s$
β	Fraction of Stokes wave	$0,78$
ρ_0	Mean value of the density	$2.2\ kg/dm^3$
L	Length of the BFR	110 m

For a sake of clarity, we first recall the formalism used in [27]. The three waves describing the stimulated Brillouin scattering in the BFR correspond to the pump electric field, the backward Stokes electric field and the density wave amplitude noted respectively E_P , E_S and ρ. They are written as [28]

$$E_P = \frac{1}{2}\tilde{A_P}(t,z)\exp^{i(\omega_P t - k_P z)} + c.c.\ , \tag{1a}$$

$$E_S = \frac{1}{2}\tilde{A_S}(t,z)\exp^{i(\omega_S t + k_S z)} + c.c.\ , \tag{1b}$$

$$\rho = \rho_0 + \frac{1}{2}\tilde{\rho}(t,z)\exp^{i(\omega t - kz)} + c.c.\ . \tag{1c}$$

In these expressions $\tilde{A_{P,S}}$ represent the complex amplitudes and $\omega_{P,S}$ the optical angular frequencies, $k_{P,S}$ the wave vectors for the pump and Stokes fields respectively. ρ_0 accounts for the mean value of the density, $\tilde{\rho}$ the amplitude, ω the angular frequency and k the wave vector for the density wave. The total optical field in the resonator $E = E_P + E_S$ and the density wave ρ are derived from the following d'Alembert and acoustic wave propagation equations:

$$\Delta E - \frac{n^2}{c^2}\frac{\partial^2 E}{\partial t^2} = \frac{1}{\varepsilon_0 c^2}\frac{\partial^2 P_{NL}}{\partial t^2}\ , \tag{2a}$$

$$\frac{\partial^2 \rho}{\partial t^2} - \Gamma\Delta(\frac{\partial \rho}{\partial t}) - v^2\Delta\rho = div\Big(\overrightarrow{grad}\big(-\frac{\varepsilon_0\gamma_e}{2}\langle E^2\rangle\big)\Big)\ . \tag{2b}$$

In these equations, P_{NL} stands for the nonlinear part of the electric polarization, n is the refractive index of the fiber, c is the celerity of light, ϵ_0 is the dielectric permittivity of vacuum, Γ is a parameter specifying the damping of the acoustic wave, v the velocity of sound in the fiber and γ_e the electrostrictive constant. Moreover, energy conservation and phase-matching for the counterpropagating pump and Stokes waves impose $\omega = \omega_P - \omega_S$ and $k = k_P + k_S$. The nonlinear part of the polarization reads [28]:

$$P_{NL} = \frac{\varepsilon_0\gamma_e}{\rho_0}\rho E\ . \tag{3}$$

Combining the previous sets of equations and calculating all the spatial and temporal derivatives for the three waves under consideration, one ends up with the following system of three equations describing the evolution of the complex amplitudes:

$$\frac{\partial \tilde{A_P}}{\partial t} + \frac{c}{n_0}\frac{\partial \tilde{A_P}}{\partial z} = -\frac{n_{loss}\omega_P}{n_0}\tilde{A_P} - \frac{i\gamma_e\omega_P}{4\rho_0 n_0^2}\tilde{A_S}\tilde{\rho}\ , \tag{4a}$$

$$\frac{\partial \tilde{A_S}}{\partial t} - \frac{c}{n_0}\frac{\partial \tilde{A_S}}{\partial z} = -\frac{n_{loss}\omega_S}{n_0}\tilde{A_S} - \frac{i\gamma_e\omega_S}{4\rho_0 n_0^2}\tilde{A_P}\tilde{\rho}^*\ , \tag{4b}$$

$$\frac{\partial \tilde{\rho}}{\partial t} + \frac{v^2 k}{\omega}\frac{\partial \tilde{\rho}}{\partial z} = -\big(\frac{\Gamma k^2}{2} + i\frac{\omega^2 - \Omega_b^2}{2\omega}\big)\tilde{\rho} - \frac{ik^2\varepsilon_0\gamma_e}{2\omega}\tilde{A_P}\tilde{A_S}^*\ , \tag{4c}$$

where a complex refractive index $n^2 = n_0^2 - 2in_0 n_{loss}$ has been introduced to take the propagation losses into account. Ω_b is the acoustic angular frequency corresponding to the highest SBS gain. Here, the transverse mode-overlap is assumed to be perfect inside the fiber, i.e. equal to unity, and we have also supposed that the complex amplitudes fulfill the slowly varying amplitude approximation.

The peculiar architecture of our resonator combined with the fact that the pump wave is going to be phase locked to the Stokes wave leads us to use appropriate hypotheses. First, as the fiber resonator is long, we keep the space variable z in order to model rigorously the Stokes optical power at the output of the resonator. Moreover, the phase-locked loop, which is designed to avoid mode hopping, will automatically position the Stokes wave frequency at the maximum Brillouin gain so that $\omega = \Omega_b$. Finally, and most importantly the fiber resonator is non-reciprocal so that it is not resonant for the pump wave, but resonant for the Stokes wave leading to peculiar boundary conditions. To solve the previous system of equations taking into account both distributed and localized losses, we introduce two different effective time constants τ_P and τ_S for the pump and Stokes waves inside the resonator:

$$\tau_{P,S} = \frac{n_0}{n_{loss}^{P,S}\omega_{P,S}}\ . \tag{5}$$

This strategy enables to push up the analytical description of the system without relying on numerical simulation. In practice the pump wave experiences propagation losses in the fiber before being abruptly evacuated by the optical circulator. The time constant τ_P encompasses distributed losses as well as the fact that the remaining pump wave after one round trip is evacuated by the circulator. Its value is inversely proportional to an effective complex refractive index denoted n_{loss}^P. In the same way, we introduce the effective time constant τ_S for the backward Stokes wave which accounts for propagation losses and localized losses at the output coupler and circulator. It is inversely proportional to an effective complex refractive index denoted n_{loss}^S. In architectures using resonant pumping the time constants for the pump and Stokes waves are nearly equal. In our case the fact that pump and Stokes waves encounter significantly different losses implies that τ_P is possibly orders of magnitude lower than τ_S. Considering all the previous hypotheses, Eqs. (4) become:

$$\frac{\partial \tilde{A_P}}{\partial t} + \frac{c}{n_0}\frac{\partial \tilde{A_P}}{\partial z} = -\frac{\tilde{A_P}}{\tau_P} - \frac{i\gamma_e\omega_P}{4\rho_0 n_0^2}\tilde{A_S}\tilde{\rho}\ , \tag{6a}$$

$$\frac{\partial \tilde{A_S}}{\partial t} - \frac{c}{n_0}\frac{\partial \tilde{A_S}}{\partial z} = -\frac{\tilde{A_S}}{\tau_S} - \frac{i\gamma_e\omega_S}{4\rho_0 n_0^2}\tilde{A_P}\tilde{\rho}^*\ , \tag{6b}$$

$$\frac{\partial \tilde{\rho}}{\partial t} + \frac{v^2 k}{\Omega_b}\frac{\partial \tilde{\rho}}{\partial z} = -\frac{\Gamma k^2}{2}\tilde{\rho} - \frac{ik^2\varepsilon_0\gamma_e}{2\Omega_b}\tilde{A_P}\tilde{A_S}^*\ . \tag{6c}$$

First, we solve the previous system of equations in the steady state, i.e. all temporal derivatives are set to zero. According to [27], the derivative of $\tilde{\rho}$ over the direction z can also be dropped, leading to the acoustic amplitude expression:

$$\tilde{\rho} = -i\frac{\varepsilon_0\gamma_e}{\Omega_b\Gamma}\tilde{A_P}\tilde{A_S}^* \tag{7}$$

At this step the expression of $\tilde{\rho}$ is injected in the equations representing the evolution of $\tilde{A_P}$ and $\tilde{A_S}$ leading to the coupled equations for the pump and Stokes powers $P_{P,S} = n_0\varepsilon_0 c S_{cf}|A_{P,S}|^2$:

$$\frac{dP_P}{dz} = -\frac{n_0}{c\tau_P}P_P - \frac{\gamma_e^2\omega_P}{4\Omega_b\Gamma\rho_0 c^2 n_0^2 S_{cf}}P_P P_S\ , \tag{8a}$$

$$\frac{dP_S}{dz} = \frac{n_0}{c\tau_S}P_S - \frac{\gamma_e^2\omega_S}{4\Omega_b\Gamma\rho_0 c^2 n_0^2 S_{cf}}P_P P_S\ , \tag{8b}$$

where S_{cf} is the mode field section. These equations are solved numerically taking in consideration the non reciprocal geometry of the resonator whose boundary conditions are:

$$P_P(z=0,m) = P_{P0} \ , \tag{9a}$$
$$P_S(z=0,m) = \beta P_S(z=L,m-1) \ , \tag{9b}$$

where m accounts for the m^{th} roundtrip inside the resonator. L is the length of the fiber and β the fraction of the Stokes wave being fed back. Figure 2 shows the comparison between the model prediction and measurements performed with our setup. The considered pump and backward Stokes powers are measured at $z = L$ and at $z = 0$, respectively. As expected the Stokes wave grows with the injected pump power above the threshold. However, the behavior of the pump wave is peculiar. Indeed, above the Brillouin threshold we observe a decrease of the transmitted pump power. The numerical model taking the variable z into account is well suited to describe the transmitted pump decrease, unlike usual models which assume the transmitted pump power to be constant above the Brillouin threshold. This numerical simulation enables us to determine precisely the photon lifetimes τ_B and τ_F that will be injected in the following analytical model. It is worthwhile mentioning that in our case τ_B and τ_F are different and that this aspect has to be considered in the model .

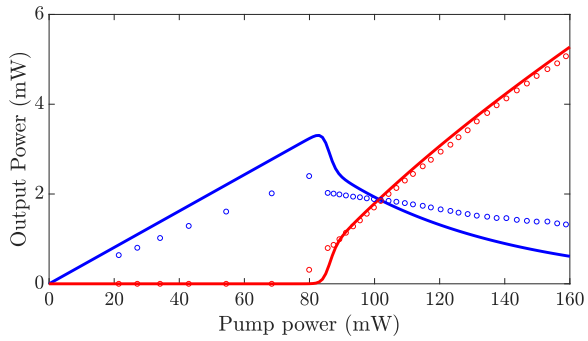

Fig. 2. Stationary state evolution of the Stokes (red) and pump (blue) powers at the cavity output as function of input pump power. Full line: model. Dotted line: experiment.

The following sections are devoted to the modeling of the whole system in terms of amplitude and frequency noise starting with the BFR.

III. Full transfer function of the system

The aim of this section is to determine the response of the system to the pump field fluctuations. Moreover, for the sack of simplicity, we want our model to rely on an analytical description. Accordingly, we are going to consider two transfer functions, one describing the amplitude and one describing the phase. These transfer functions are coupled due to amplitude to phase conversion occurring. The two loops that we consider are schematized on Figure 3.

The phase loop (in blue) is closed and fed by two noise sources, namely $\delta\varphi_{LO}$ and $\delta\varphi_L$ corresponding to the phase

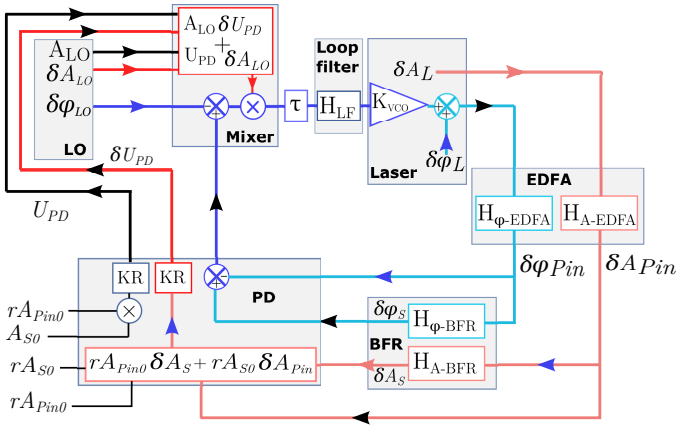

Fig. 3. Scheme of the two-loop transfert model, consisting of seven elements: Erbium doped fiber amplifier (EDFA), Brillouin fiber resonator (BFR), photodiode (PD): KR stands for the product of responsivity by load, local RF oscillator (LO), mixer, pure delay (τ), loop filter, laser. Blue loop: phase variations. Red loop: amplitude variations. Dark: mean values. Light color: optical fields. Dark color: electric signals.

fluctuations of the local oscillator and pump laser wave respectively. Conversely, the amplitude loop (in red) is open. The amplitude fluctuations of the local oscillator the laser δA_{LO} and δA_L, act as noise sources. The transfer function of each element, i.e. BFR, EDFA, PD, mixer, loop filter, delay and laser (see Fig. 3), can be obtained from a linearization of their time response, as it will now be discussed.

A. Brillouin fiber resonator

The time response of BFR is governed by the set of coupled-mode equations (Eqs. 6). As we focus on a precise location inside the fiber resonator, the spatial derivatives are set to zero. A pumping term proportional to the input pump complex amplitude $\tilde{A_{Pin}}$ has then to be added to the pump wave evolution equation (Eq 6a). A phenomenological time τ_{ext} is introduced to take into account the input coupler transmission. The pumping term then reads $\tilde{A}_{Pin}/\tau_{ext}$. Finally, we separate scalar amplitudes and phases:

$$\tilde{A}_{P,S,Pin} = A_{P,S,Pin} e^{i\varphi_{P,S,Pin}} \quad , \quad \tilde{\rho} = \rho e^{i\varphi} \ , \tag{10}$$

and we consider small variations around the steady-state values:

$$A_{P,S,Pin} = A_{P0,S0,Pin0} + \delta A_{P,S,Pin} \ , \tag{11a}$$
$$\varphi_{P,S,Pin} = \varphi_{P0,S0,Pin0} + \delta\varphi_{P,S,Pin} \ , \tag{11b}$$
$$\rho = \rho_{00} + \delta\rho \ , \tag{11c}$$
$$\varphi = \varphi_0 + \delta\varphi \ . \tag{11d}$$

The steady state solutions can be retrieved from Eqs. (6). In particular, one gets:

$$\varphi_{P0} - \varphi_{S0} - \varphi_0 = \frac{\pi}{2} \ . \tag{12}$$

Moreover, assuming that $\varphi_{Pin0} - \varphi_{P0} = 0$, we end up with the following equation system:

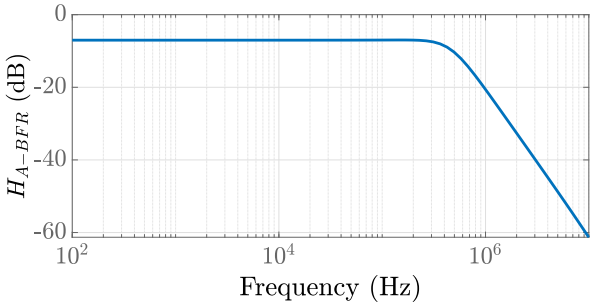

Fig. 4. Theoretical pump to Stokes amplitude noise transfer function of the Brillouin fiber resonator

$$\frac{\partial \delta A_P}{\partial t} = -\frac{\delta A_P}{\tau_P} - \frac{\omega_P \gamma_e}{4\rho_0 n_0^2}(A_{S0}\delta\rho + \delta A_S \rho_{00}) + \frac{\delta A_{Pin}}{\tau_{ext}} \ , \tag{13a}$$

$$\frac{\partial \delta A_S}{\partial t} = -\frac{\delta A_S}{\tau_S} + \frac{\omega_S \gamma_e}{4\rho_0 n_0^2}(A_{P0}\delta\rho + \delta A_P \rho_{00}) \ , \tag{13b}$$

$$\frac{\partial \delta\rho}{\partial t} = -\frac{\Gamma k^2}{2}\delta\rho + \frac{k^2\varepsilon_0\gamma_e}{2\omega}(A_{P0}\delta A_S + A_S 0 \delta A_P) \ , \tag{13c}$$

$$\begin{aligned}\frac{\partial \varphi_P}{\partial t} &= \frac{\omega_P \gamma_e A_{S0}\rho_{00}}{4\rho_0 n_0^2 A_{P0}}(\delta\varphi_P - \delta\varphi_S - \delta\varphi) \\ &+ \frac{A_{Pin0}}{\tau_{ext}A_{P0}}(\delta\varphi_{P_{in}} - \delta\varphi_P)\end{aligned} \ , \tag{13d}$$

$$\frac{\partial \varphi_S}{\partial t} = \frac{\omega_S \gamma_e A_{P0}\rho_{00}}{4\rho_0 n_0^2 A_{S0}}(\delta\varphi_P - \delta\varphi_S - \delta\varphi) \ , \tag{13e}$$

$$\frac{\partial \varphi}{\partial t} = \frac{k^2\varepsilon_0\gamma_e A_{S0}A_{P0}}{2\omega\rho_{00}}(\delta\varphi_P - \delta\varphi_S - \delta\varphi) \ . \tag{13f}$$

showing that the amplitude and phase fluctuations are uncoupled. Thus, we can write the set of Eqs.(13) as:

$$\begin{bmatrix} \frac{\partial \delta A_P}{\partial t} \\ \frac{\partial \delta A_S}{\partial t} \\ \frac{\partial \delta\rho}{\partial t} \end{bmatrix} = \mathbf{M}_A \begin{bmatrix} \delta A_P \\ \delta A_S \\ \delta\rho \end{bmatrix} + \begin{bmatrix} \frac{\delta A_{Pin}}{\tau_{ext}} \\ 0 \\ 0 \end{bmatrix} \ , \tag{14}$$

$$\begin{bmatrix} \frac{\partial \delta\varphi_P}{\partial t} \\ \frac{\partial \delta\varphi_S}{\partial t} \\ \frac{\partial \delta\varphi}{\partial t} \end{bmatrix} = \mathbf{M}_\varphi \begin{bmatrix} \delta\varphi_P \\ \delta\varphi_S \\ \delta\varphi \end{bmatrix} + \begin{bmatrix} \frac{A_{Pin0}}{\tau_{ext}A_{P0}}\delta\varphi_{Pin} \\ 0 \\ 0 \end{bmatrix} \ , \tag{15}$$

where the matrices $\mathbf{M}_A$ and $\mathbf{M}_\varphi$ are equal to

$$\mathbf{M_A} = \begin{pmatrix} -\frac{1}{\tau_P} & -C_1\omega_P\rho_{00} & -C_1\omega_P A_{S0} \\ C_1\omega_S\rho_{00} & -\frac{1}{\tau_S} & C_1\omega_S A_{P0} \\ C_2 A_{S0} & C_2 A_{P0} & -\frac{1}{\tau_B} \end{pmatrix} \ , \tag{16a}$$

$$\mathbf{M}_\varphi = \begin{pmatrix} -K_4 & -K_1 & -K_1 \\ K_2 & -K_2 & -K_2 \\ K_3 & -K_3 & -K_3 \end{pmatrix} \ , \tag{16b}$$

with the parameters defined as

$$\begin{aligned} &C_1 = \frac{\gamma_e}{4\rho_0 n_0^2} \ , \qquad C_2 = \frac{k^2\varepsilon_0\gamma_e}{2\omega} \ , \qquad \tau_B = \frac{1}{\Gamma k^2} \ , \\ &K_1 = \frac{\omega_P\gamma_e A_{S0}\rho_{00}}{4\rho_0 n_0^2 A_{P0}} \ , \qquad K_2 = \frac{\omega_S\gamma_e A_{P0}\rho_{00}}{4\rho_0 n_0^2 A_{S0}} \ , \\ &K_3 = \frac{k^2\varepsilon_0\gamma_e A_{S0}A_{P0}}{2\omega\rho_0} \ , \qquad K_4 = \frac{A_{Pin0}}{A_{P0}\tau_{ext}} - K_1 \ . \end{aligned} \tag{17}$$

Both systems (14) and (12) can be solved in the frequency domain, leading to the variations of the Stokes wave versus pump fluctuations. This leads to the amplitude and phase transfer functions, labelled $H_{A-BFR}(s) = \frac{\delta A_S(s)}{\delta A_{Pin}(s)}$ and $H_{\varphi-BFR}(s) = \frac{\delta\varphi_S(s)}{\delta\varphi_{Pin}(s)}$ respectively.

s stands for the Laplace variable $s = i2\pi f$. These transfer functions write as:

$$H_{A-BFR} = \frac{A_{S0}}{\tau_S\tau_{ext}A_{P0}}\frac{s + C_3}{s^3 + C_4 s^2 + C_5 s + C_6} \ , \tag{18}$$

and

$$H_{\varphi-BFR} = K_2(K_1 + K_4)\frac{s + K_3}{s^3 + K_5 s^2 + K_6 s + K_7} \ , \tag{19}$$

with

$$\begin{aligned} &C_3 = \frac{2}{\tau_B} \ , \qquad C_4 = \frac{1}{\tau_P} + \frac{1}{\tau_S} + \frac{1}{\tau_B} \ , \\ &C_5 = (\frac{1}{\tau_S} + \frac{1}{\tau_B})(\frac{1}{\tau_P} + \frac{\omega_P A_{S0}^2}{\tau_S\omega_S A_{P0}^2}) \ , \qquad C_6 = \frac{4\omega_P A_{S0}^2}{\tau_B\tau_S^2\omega_S A_{P0}^2} \ , \\ &K_5 = K_2 + 2K_3 + K_4 \ , \\ &K_6 = (K_2 + 2K_3)(K_1 + K_4) + K_1 K_2 \ , \\ &K_7 = K_3(K_2 + K_3)(K_1 + K_4) \ . \end{aligned} \tag{20}$$

Figure 4 illustrates the Bode diagram corresponding to the magnitude $|H_{A-BFR}|$ of the amplitude transfer function. The numerical values of the relevant parameters have been extracted from table 1. This Bode diagram shows that BFR acts as a second-order low-pass filter for the amplitude fluctuations.

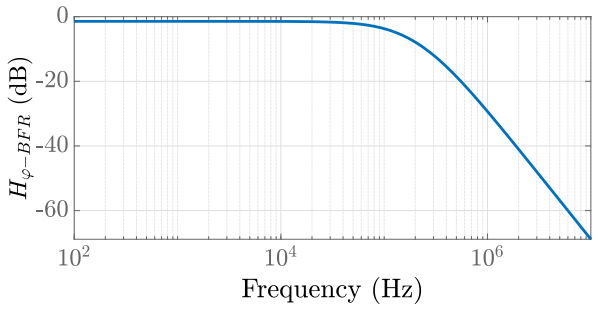

Fig. 5. Theoretical pump to Stokes phase noise transfer function of the Brillouin fiber resonator.

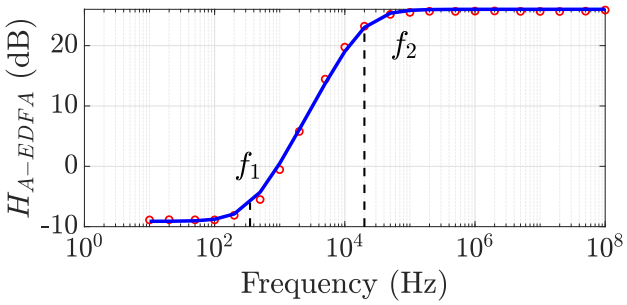

Fig. 6. Transfer function of the EDFA relative to amplitude noise. Blue: Model. Red: Experiment.

Figure 5 shows the Bode diagram associated with the amplitude of the phase transfer function $|\varphi_{A-BFR}|$. The Brillouin resonator also responds to phase fluctuations of its pump as a second order low pass filter which rejects high frequency perturbations whatever their nature. The Stokes signal out of the resonator is then naturally less noisy than its pump regarding all types of noises above the cut-off frequency, here at around 2 MHz.

B. Erbium-doped fiber amplifier

The use of an Erbium-doped fiber amplifier (EDFA) is mandatory when the pump laser power is lower than the Brillouin fiber laser threshold which corresponds to 90 mW in our setup. The EDFA having a low phase-noise figure, we neglect its additional contribution to the full system phase noise [29]. Accordingly we consider that:

$$H_{\varphi-EDFA} = 1 \ , \tag{21}$$

Conversely the EDFA response to amplitude fluctuations must be carefully taken into account due to coherent population oscillations (CPO) effect [30]. Indeed, under saturation, the optical gain varies with the input optical power at low frequency. Low power fluctuations will experience a high gain while high input power fluctuations will experience low gain. Then, under a cut-off frequency f_1 given by the upper level lifetime, the intensity variations of the incoming beam will be almost annihilated. Conversely, above a second cut-off frequency f_2 given by the upper level lifetime and the gain compression coefficient, the intensity variations are amplified [31]. The EDFA will then act as a high pass filter. Regarding the response of the EDFA can be modeled as a limited derivator transfer function that reads:

$$H_{A-EDFA}(s) = G_{opt}\frac{f_1}{f_2}\frac{1+\dfrac{s}{2\pi f_1}}{1+\dfrac{s}{2\pi f_2}} \ , \tag{22}$$

where f_1 and f_2 are measured experimentally. Figure 6 shows the experimental response of our EDFA from which $f_1 = 350Hz$, $f_2 = 20kHz$ and the optical gain $G_{opt} = 20$ are extracted.

Although the main goal of the optical amplifier is to exceed the Brillouin threshold, it is noticeable that it will also provide significant amplitude noise attenuation at low frequencies.

C. Photodiode

An AC fast photodiode PD, here 10 GHz cut-off frequency, is used to generate the pump/Stokes beatnote signal. Introducing r, the ratio of pump impinging on PD, the produced photocurrent can be written as $i_{PD} = K|\sqrt{r}E_{Pin}+E_S|^2$ with K a constant coefficient.

Neglecting second order terms, the output voltage reads

$$u_{PD} = (U_{PD0}+\delta U_{PD0})cos((\omega_P-\omega_S)t+\varphi_{Pin}-\varphi_S) \ , \tag{23}$$

with

$$U_{PD0} = \sqrt{r}RKA_{Pin0}A_{S0} \ , \tag{24}$$

and

$$\delta U_{PD0} = \sqrt{r}RK(A_{Pin0}\delta A_S + A_S\delta A_{Pin0}) \ . \tag{25}$$

R is the effective output load at the beating frequency. In our setup, r, K and R are equal to 0.1, 0.95 and 50 Ω, respectively. We point out that u_{PD} is the OPLL output signal. Its phase noise is the difference of the Stokes and pump waves phase noises while its amplitude noise is a linear combination of the Stokes and pump amplitude noises weighted by their mean amplitudes.

D. Mixer

A mixer is used to compare the pump/Stokes beatnote to the frequency reference provided by a RF local oscillator. The voltage input reads

$$u_{LO} = (U_{LO}+\delta U_{LO})sin(\omega_{LO}t+\varphi_{LO}) \ , \tag{26}$$

The output of the mixer u_{mix} corresponds to the PLL error voltage which is proportionnal to the phase difference $\varphi_{PD}-\varphi_S-\varphi_{LO}$:

$$\begin{aligned} u_{mix} =& K_{comp}(U_{PD0}+\delta U_{PD0})(U_{LO}+\delta U_{LO}) \\ &\times(\varphi_{PD}-\varphi_S-\varphi_{LO}) \ . \end{aligned} \tag{27}$$

K_{comp} was measured to be 0.71 V^{-1}. This result has been obtained after considering the locking of the PLL, that is $\omega_P-\omega_S=\omega_{LO}$ and $(\varphi_{PD}-\varphi_S)-\varphi_{LO} \ll \pi$. Moreover, the terms at frequencies higher than 1 MHz have been neglected. Eq.(27) shows that the error signal is also impacted by amplitude fluctuations of the photodiode and local oscillator

voltages, leading to amplitude-to-phase conversion. This may increase the pump laser phase noise. Consequently, in order to maximize the system efficiency, the pump laser amplitude noise must be limited.

E. Loop filter and delay

The baseband signal coming out of the mixer goes through an electronical loop filter. This filter ensures the system stability while globally improving the PLL performances. We choose to design a filter with two poles and two zeros. The transfer function H_{LF} of the loop filter is given by:

$$H_{LF}(s) = G_{elec} \frac{1+\frac{s}{2\pi f_3}}{1+\frac{s}{2\pi f_4}} \frac{1+\frac{s}{2\pi f_5}}{1+\frac{s}{2\pi f_6}} \ . \tag{28}$$

In this expression G_{elec} is the steady state electrical gain. Figure 7 presents both theoretical and experimental magnitude of the transfer function of our filter.

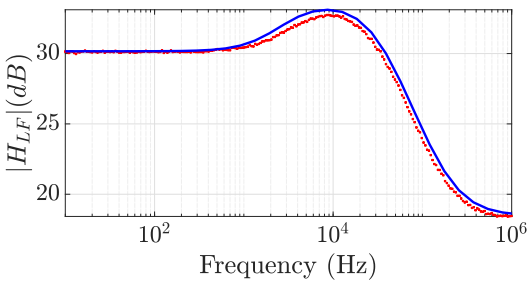

Fig. 7. Bode diagram of the loop filter. The poles frequencies are $f_3 = 3.12kHz$ and $f_5 = 32.7kHz$ whereas the zeros frequencies are $f_4 = 2.08kHz$ and $f_6 = 188.6kHz$. Blue: Model. Red: Experiment.

We also introduce in the model a pure-delay line accounting for the total length of the loop (optical and electrical parts), corresponding to a transfer function:

$$H_{delay}(s) = e^{-\tau s} \ , \tag{29}$$

where $\tau = 1.66.10^{-7}$ s.

F. Pump laser as a VCOO

We remind that the pump laser is acting as a VCOO. The voltage out of the loop filter is applied on an intra-cavity Kerr electro-optical crystal to slightly change the cavity length and consequently the pump laser frequency. The crystal response can be considered to be linear, due to the low value of voltage corrections. It leads to a modification of the instantaneous optical angular frequency $\omega_L = K_{VCOO} V_{LF} + \omega_0$ with ω_0 the laser angular frequency without correction. Considering the phase as the signal of interest out of the VCOO, the transfer function reads:

$$H_{VCOO}(s) = \frac{K_{VCOO}}{s} \ . \tag{30}$$

In our setup, K_{VCOO} was measured to be equal to $80\pi 10^6 rad.s^{-1}.V^{-1}$. Finally, we also introduce two inputs $\delta\varphi_L$ and δA_L accounting for the pump laser phase and amplitude fluctuations in free running.

In brief, the aim of this section was to theoretically describe the whole setup as a series of amplitude and phase transfert functions. We point out that our model allows one to explore the fundamental limits of the photonic oscillator as it includes the noise contributions of the different components. For instance, the model predicts that the amplitude noise of the pump laser has an important role as it impacts directly the frequency noise of the oscillator. The frequency noise of the local oscillator has also a contribution but its impact is less important. In order to ensure the validity of our approach, we now compare the model prediction with measured transfer functions, as will be discussed in the next section.

IV. Experiments vs model

The transfer function of the full setup can be measured by opening the loop, e.g., after the mixer. The elements successively encountered are the time delay, the loop filter, the laser, the photodiode, the Brillouin resonator for associated part of the signal, the photodiode and the mixer. The theoretical open loop transfer function is:

$$\begin{aligned} H_{open}(s) =& \sqrt{r} R K K_{comp} H_{LF}(s)(1 - H_{\varphi-BFR}(s)) \\ & \times \frac{K_{VCOO}}{s} e^{-\tau s} \ . \end{aligned} \tag{31}$$

However, the characterization of the corresponding experimental open loop transfer function is fairly difficult because while the loop is open, the system experiences mode-hops. It is thus mandatory to keep the loop physically closed during the measurements.

A. Open loop transfer function measurements

To measure the open loop transfer function, a small controlled voltage perturbation $P(\omega)$ at angular frequency ω is added right after the mixer, as shown on Figure 8. It induces a small signal ε_1 out of the mixer. We write $\varepsilon_2 = \varepsilon_1 + P$ and $\varepsilon_3 = H_{LF}\ \varepsilon_2$. Provided that P is the dominant perturbation in the system, one gets:

$$H_{open}(\omega) \simeq -\frac{\varepsilon_1}{\varepsilon_2} \ , \qquad \frac{H_{open}(\omega)}{H_{LF}(\omega)} \simeq -\frac{\varepsilon_1}{\varepsilon_3} \ . \tag{32}$$

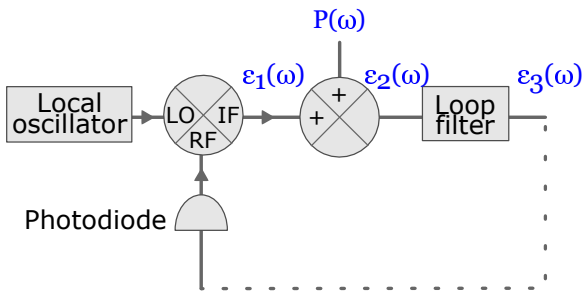

Fig. 8. Principle of the open loop transfer function measurement. $P(\omega)$: small controlled perturbation ; ε_i: induced signals.

We then monitor $\varepsilon_1(\omega)$ and $\varepsilon_2(\omega)$ using a lock-in amplifier synchronized to the input perturbation $P(\omega)$. We also monitor $\varepsilon_3(\omega)$ to get the open loop transfer function of the system without filter (see Eq.32). This last transfer function is particularly interesting because it permits to evaluate the behavior of the system independently of the loop filter. We remind that in our setup the loop filter is used as the adjustment parameter. Comparison between the model prediction and an actual measurement of the open loop transfer function without filter is reported in Figure 9. It shows a very good agreement from 8 kHz to 3 MHz, that is over more than 2 decades.

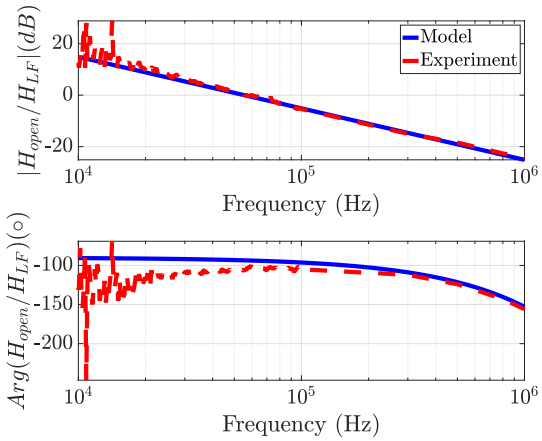

Fig. 9. Open loop transfer function measurement and model prediction. Blue: Model. Red: Experiment.

Notice that ε_3 stands for a perturbation divided by the loop gain. Due to the extremely high gain at low frequencies, the measurement of ε_3 below a few kHz was out of reach. Moreover for frequencies higher than 3 MHz, the assumption that the introduced perturbation dominates was not valid anymore. Figure 9 shows that our setup behaves as an integrator, i.e. gain slope of $-20dB/dec$ and phase shift of $-90\,\mathrm{deg}$. Around 1 MHz the phase drops due to the loop delay τ. Measurements led to estimate $\tau = 175$ ns which corresponds to propagation over 35 m. This length corresponds to the path followed by the reference pump signal going directly to the photodiode without entering the BFL, (see Figure 3). Then, we have inserted optical fibers of different lengths between the input coupler and BFR, thus varying the delay time τ' depicted on Figure 1 from 5 to 500 ns. We always observed the same experimental transfer function which does not depend on any delay time associated to BFR. As the relevant delay is only linked to the shortest path, it limits the impact of the delay on the global system stability. These results demonstrate that the Brillouin resonator transfer function does not have any impact on the open loop transfer function. Consequently and as expected, the BFR acts as an optical reference with a high spectral purity.

B. Frequency response to a step perturbation

In linear systems, the open-loop transfer function and the response to a step perturbation are theoretically equivalent. However, we have made assumptions when measuring the open-loop transfer function. In order to confirm our results, we now study how the laser optical frequency reacts to a frequency step of the LO. In practice, the frequency of our syntheziser can switch by 300 kHz step within 200 ns. This switch-time can fairly be considered as instantaneous compared to the system time constant. Thus when the synthesizer switches by 300 kHz we expect the pump laser frequency to also shift by 300 kHz. In addition relevant information about the system is contained in the transient response. To study such transient response, we used an unbalanced fibered Mach-Zehnder interferometer schematized in Figure 10.

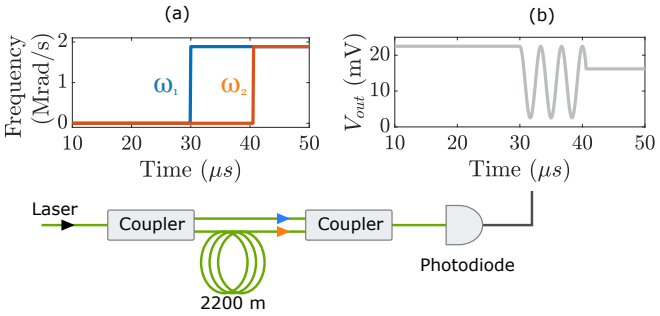

Fig. 10. Unbalanced Mach-Zehnder interferometer. Short arm: 1 m. Long arm: 2200 m. Insets. (a) Output angular frequencies for a step variation; ω_1 (blue) and ω_2 (brown) are associated to the short and long arms, respectively. (b) Corresponding output voltage.

This interferometer consists in one 1 m-long arm and one 2200-m long arm sandwiched by two 50/50 couplers. We checked that the optical losses in the two arms are negligeable. The optical field inpinging on the photodiode then reads:

$$E_{in} = \frac{E_0}{2}\left(e^{i\omega_1 t} + e^{i\omega_2(t-\tau_i)}\right) \ . \tag{33}$$

ω_1 and ω_2 are the instantaneous angular frequencies at the end of the short and long arms, respectively. $\tau_i = \Delta L/c$ refers to the interferometer delay time between the two arms, where ΔL is the optical path difference. E_0 is the input optical field. The output voltage delivered by the photodiode is then:

$$v_{out} = V_0\left(1 + cos\left(\left(\omega_1 - \omega_2\right)t + \omega_2\tau_i\right)\right) + V_{off} \ , \tag{34}$$

with V_0 a constant voltage and V_{off} an offset voltage. Figure 10 illustrates the expected time interferogram for a frequency step of 300 kHz if the system response is instantaneous, that is, angular frequencies ω_1 and ω_2 variations consist in two perfect steps. The output voltage is constant when $\omega_1 = \omega_2$ and varies at 300 kHz when $\omega_1 \neq \omega_2$. The information we intend to retrieve will be in the transient signal added to this waveform due to the system response. Figure 11 shows both theoretical and experimental interferograms.

As expected, the voltage before frequency switch is constant. The little oscillation is due to the relaxation oscillations of the laser. Then we recognize a transient behavior followed by a new constant signal. The transient signal differs from the one presented in Figure 10 due to the system time response. The step response predicted by the model is computed numerically because of its complexity. Nevertheless, a good approximation can be made by neglecting the BFR impact, the

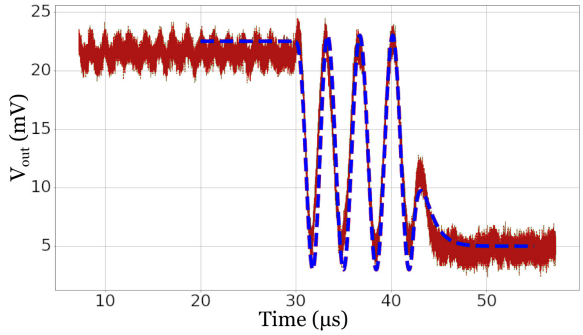

Fig. 11. Interferogram resulting from a 1 MHz frequency step on the local oscillator. Blue: Model. Red: Experiment.

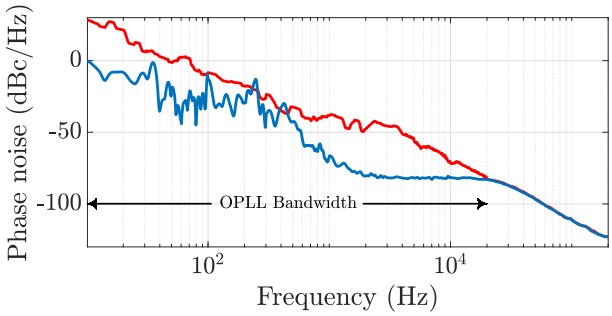

Fig. 12. Optical phase noise of the laser. Red: free running; Blue: closed-loop. See text for details

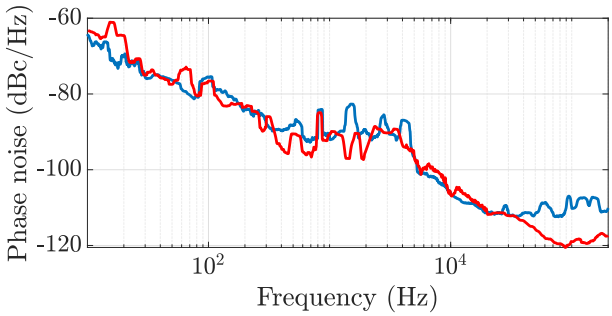

Fig. 13. Relative phase noise spectrum of the laser/stokes beat note at 10.998 GHz. Red: Model. Blue: Experiment.

delay τ and using a pure G_0 gain loop filter. The open loop transfer function of Eq. (31) then writes $H_{open}(s) = K_0/s$ with $K_0 = \sqrt{r}RKK_{comp}G_0K_{VCOO}$. This leads to the step response for the close loop:

$$f(t) = 1 - e^{-K_0 t} \ . \tag{35}$$

At the end of the interferometer arms the instantaneous frequencies are:

$$\omega_1(t) = \omega_0 + \Delta\omega(1 - e^{-K_0 t})H(t) \ , \tag{36a}$$
$$\omega_2(t) = \omega_0 + \Delta\omega(1 - e^{-K_0 t})H(t - \tau_i) \ , \tag{36b}$$

with ω_0 the initial angular frequency of the laser, $\Delta\omega$ the amplitude of the angular frequency step imposed to the local oscillator and $H(t)$ the Heaviside function. Introducing the expression (34) into Eq.(36) leads to the theoretical fit of Figure 11. Once again, the model predictions are in fairly good agreement with the experimenatl observations.

C. Phase noise

We now aim to compare the experimental phase noise level with the model predictions. In the simulations, we considered three possible noise sources, namely the pump laser, the local oscillator and the Brillouin resonator, the contribution of other noise sources being supposed to be negligible. First, the optical phase noise spectrum of the free running laser, i.e. $\delta\varphi_{LO}$, is retrieved experimentally from the output signal of the unbalanced MZM using the self-heterodyne technique [32] (see Fig. 12).

From this spectrum and the phase noise of the local oscillator $\delta\varphi_{L0}$, one can compute the closed-loop phase noise of the difference $\varphi_{Pin} - \varphi_S$ corresponding to an estimate of the phase noise associated to the beat note between the laser and the Stokes wave, the added noise due to the EDFA being supposed to be negligible (Eq. 21).

Fig. 13 compares this predicted closed loop phase noise to the recorded experimental phase noise spectrum showing again a good agreement. Note that the efficiency of the OPPL can be assessed on the closed-loop optical spectrum of Fig.12, which shows a significant reduction of the phase noise over the 20 kHz bandwidth of the feedback loop. Notice that the PPL bandwidth is not really an issue in the current configuration as it is larger than the free running linewidth of the pump laser. If the pump is replaced by a laser with a larger linewidth, such as a semiconductor laser, then the PLL bandwidth must be increased, at the expense of its gain.

V. Conclusion

In conclusion, we have developed a theoretical model describing the self-narrowed photonic oscillator including an OPLL as recently proposed. This model relies on two interleaved feedback loops. A good agreement is obtained between our model predictions and the experimental measurements, both for frequency response and phase noise level. Moreover, we show that the long Brillouin fiber loop acts as a local oscillator and that the delay associated to this loop does not enter into play in the photonic oscillator servo-locking bandwith. As our model is based on a full-analytical analysis of the whole transfer functions, it is an efficient tool for defining and optimizing the different parts of the system, using well established servo-loop calculations. This model applies to any pump laser that can be turned to a VCOO, such as, e.g., fiber DFB lasers [33], or electrically-driven semiconductor lasers by including the Henry factor in the model. Moreover this model can be extended to more sophisticated fiber SBS resonators. Finally this model will be employed to optimize more compact configurations based on silicon [34] and Si_3N_4 [35] integrated circuits, which is the next step of this work.

Fundings

This work was partly funded by Agence National de la Recherche (ANR-13-INFR-0011 project "Com'Toniq") and

Région Bretagne.

ACKNOWLEDGMENTS

The authors would like to thank François Bondu, Stéphanie Molin and Pascal Szritgiser for fruitful discussions, and Ludovic Frein for technical assistance.

REFERENCES

[1] G. M. Brodnik, M. W. Harrington, J. H. Dallyn, D. Bose, W. Zhang, L. Stern, P. A. Morton, R. O. Behunin, S. B. Papp, and D. J. Blumenthal, "Optically synchronized fibre links using spectrally pure chip-scale lasers," *Nature Photonics*, vol. 15, no. 8, pp. 588–593, Aug. 2021.

[2] M. Schioppo, J. Kronjäger, A. Silva, R. Ilieva, J. W. Paterson, C. F. A. Baynham, W. Bowden, I. R. Hill, R. Hobson, A. Vianello, M. Dovale-Álvarez, R. A. Williams, G. Marra, H. S. Margolis, A. Amy-Klein, O. Lopez, E. Cantin, H. Álvarez Martínez, R. Le Targat, P. E. Pottie, N. Quintin, T. Legero, S. Häfner, U. Sterr, R. Schwarz, S. Dörscher, C. Lisdat, S. Koke, A. Kuhl, T. Waterholter, E. Benkler, and G. Grosche, "Comparing ultrastable lasers at 7 × 10 17 fractional frequency instability through a 2220 km optical fibre network," *Nature Communications*, vol. 13, no. 1, p. 212, Jan. 2022.

[3] J. Capmany, J. Mora, I. Gasulla, J. Sancho, J. Lloret, and S. Sales, "Microwave Photonic Signal Processing," *Journal of Lightwave Technology*, vol. 31, no. 4, pp. 571–586, Feb. 2013.

[4] T. Tetsumoto, T. Nagatsuma, M. E. Fermann, G. Navickaite, M. Geiselmann, and A. Rolland, "300 GHz wave with attosecond-level timing noise," *Nature Photonics*, vol. 15, no. 7, pp. 516–522, Jul. 2021.

[5] K. Kikuchi, "Fundamentals of Coherent Optical Fiber Communications," *Journal of Lightwave Technology*, vol. 34, no. 1, pp. 157–179, Jan. 2016.

[6] M. Yoshida, T. Kan, K. Kasai, T. Hirooka, K. Iwatsuki, and M. Nakazawa, "10 Channel WDM 80 Gbit/s/ch, 256 QAM Bi-Directional Coherent Transmission for a High Capacity Next-Generation Mobile Fronthaul," *Journal of Lightwave Technology*, vol. 39, no. 5, pp. 1289–1295, Mar. 2021.

[7] W. Loh, J. Stuart, D. Reens, C. D. Bruzewicz, D. Braje, J. Chiaverini, P. W. Juodawlkis, J. M. Sage, and R. McConnell, "Operation of an optical atomic clock with a Brillouin laser subsystem," *Nature*, vol. 588, no. 7837, pp. 244–249, Dec. 2020.

[8] N. Bode, J. Briggs, X. Chen, M. Frede, P. Fritschel, M. Fyffe, E. Gustafson, M. Heintze, P. King, J. Liu, J. Oberling, R. L. Savage, A. Spencer, and B. Willke, "Advanced LIGO Laser Systems for O3 and Future Observation Runs," *Galaxies*, vol. 8, no. 4, p. 84, Dec. 2020. [Online]. Available: https://www.mdpi.com/2075-4434/8/4/84

[9] T. J. Kane and R. L. Byer, "Monolithic, unidirectional single-mode Nd:YAG ring laser," *Optics Letters*, vol. 10, no. 2, p. 65, Feb. 1985.

[10] S. Fu, W. Shi, Y. Feng, L. Zhang, Z. Yang, S. Xu, X. Zhu, R. A. Norwood, and N. Peyghambarian, "Review of recent progress on single-frequency fiber lasers," *Journal of the Optical Society of America B*, vol. 34, no. 3, p. A49, Mar. 2017.

[11] L. Ricci, M. Weidemuller, T. Esslinger, C. Zimmermann, and T. Hansch, "A compact grating-stabilized diode laser system for atomic physics," *Optics communication*, vol. 117, no. 2, pp. 541–549, Jun. 1995.

[12] B. Mroziewicz, "External cavity wavelength tunable semiconductor lasers - a review," *Opto-Electronics Review*, vol. 16, no. 4, Jan. 2008.

[13] P. Laurent, A. Clairon, and C. Breant, "Frequency noise analysis of optically self-locked diode lasers," *IEEE Journal of Quantum Electronics*, vol. 25, no. 6, pp. 1131–1142, 1989.

[14] NKT-Photonic, "Koheras BASIK single frequency fiber lasers," 2023, https://www.nktphotonics.com/.

[15] OEwaves, "HI-Q LASERS Series," 2023, https://www.oewaves.com/.

[16] D. Matei, T. Legero, S. Häfner, C. Grebing, R. Weyrich, W. Zhang, L. Sonderhouse, J. Robinson, J. Ye, F. Riehle, and U. Sterr, "1.5 micron Lasers with Sub-10 mHz Linewidth," *Physical Review Letters*, vol. 118, no. 26, p. 263202, Jun. 2017.

[17] M. De Labachelerie, C. Latrasse, K. Diomande, P. Kemssu, and P. Cerez, "A 1.5 micron absolutely stabilized extended-cavity semiconductor laser," *IEEE Transactions on Instrumentation and Measurement*, vol. 40, no. 2, pp. 185–190, Apr. 1991.

[18] A. Kobyakov, M. Sauer, and D. Chowdhury, "Stimulated Brillouin scattering in optical fibers," *Advances in Optics and Photonics*, vol. 2, no. 1, p. 1, Mar. 2010.

[19] S. P. Smith, F. Zarinetchi, and S. Ezekiel, "Narrow-linewidth stimulated Brillouin fiber laser and applications," *Optics Letters*, vol. 16, no. 6, p. 393, Mar. 1991.

[20] A. Debut, S. Randoux, and J. Zemmouri, "Experimental and theoretical study of linewidth narrowing in brillouin fiber ring lasers," vol. 18, no. 4, p. 556. [Online]. Available: https://opg.optica.org/abstract.cfm?URI=josab-18-4-556

[21] J. Geng, S. Staines, and S. Jiang, "Dual-frequency Brillouin fiber laser for optical generation of tunable low-noise radio frequency/microwave frequency," *Optics Letters*, vol. 33, no. 1, p. 16, Jan. 2008.

[22] S. Kato and T. Aoki, "Single-frequency fiber fabry–perot brillouin laser," vol. 47, no. 19, p. 5000. [Online]. Available: https://opg.optica.org/abstract.cfm?URI=ol-47-19-5000

[23] G. Danion, L. Frein, D. Bacquet, G. Pillet, S. Molin, L. Morvan, G. Ducournau, M. Vallet, P. Szriftgiser, and M. Alouini, "Mode-hopping suppression in long Brillouin fiber laser with non-resonant pumping," *Optics Letters*, vol. 41, no. 10, p. 2362, May 2016.

[24] S. Norcia, S. Tonda-Goldstein, D. Dolfi, J.-P. Huignard, and R. Frey, "Efficient single-mode Brillouin fiber laser for low-noise optical carrier reduction of microwave signals," *Optics Letters*, vol. 28, no. 20, p. 1888, Oct. 2003.

[25] T. Carmon, L. Yang, and K. J. Vahala, "Dynamical thermal behavior and thermal selfstability of microcavities."

[26] G. Danion, M. Vallet, L. Frein, P. Szriftgiser, and M. Alouini, "Brillouin Assisted Optoelectronic Self-Narrowing of Laser Linewidth," *IEEE Photonics Technology Letters*, vol. 31, no. 12, pp. 975–978, Jun. 2019.

[27] W. Loh, S. B. Papp, and S. A. Diddams, "Noise and dynamics of stimulated-Brillouin-scattering microresonator lasers," *Physical Review A*, vol. 91, no. 5, p. 053843, May 2015.

[28] R. Boyd and D. Prato, *Nonlinear Optics*. Elsevier Science, 2008. [Online]. Available: https://books.google.fr/books?id=uoRUi1Yb7ooC

[29] E. Rochat and R. Dandliker, "New investigations on the effect of fiber amplifier phase noise," *IEEE Journal of Selected Topics in Quantum Electronics*, vol. 7, no. 1, pp. 49–54, Feb. 2001.

[30] G. Danion, F. Bondu, G. Loas, and M. Alouini, "GHz bandwidth noise eater hybrid optical amplifier: design guidelines," *Optics Letters*, vol. 39, no. 14, p. 4239, Jul. 2014.

[31] R. Boula-Picard, M. Alouini, J. Lopez, N. Vodjdani, and J.-C. Simon, "Impact of the gain saturation dynamics in semiconductor optical amplifiers on the characteristics of an analog optical link," *Journal of Lightwave Technology*, vol. 23, no. 8, pp. 2420–2426, Aug. 2005.

[32] O. Llopis, P. H. Merrer, H. Brahimi, K. Saleh, and P. Lacroix, "Phase noise measurement of a narrow linewidth CW laser using delay line approaches," *Optics Letters*, vol. 36, no. 14, p. 2713, Jul. 2011.

[33] K. H. Tow, Y. Léguillon, S. Fresnel, P. Besnard, L. Brilland, D. Méchin, D. Trégoat, J. Troles, and P. Toupin, "Linewidth-narrowing and intensity noise reduction of the 2nd order Stokes component of a low threshold Brillouin laser made of $Ge_{10}As_{22}Se_{68}$ chalcogenide fiber," *Optics Express*, vol. 20, no. 26, 2012.

[34] B. Morrison, A. Casas-Bedoya, G. Ren, K. Vu, Y. Liu, A. Zarifi, T. G. Nguyen, D.-Y. Choi, D. Marpaung, S. J. Madden, A. Mitchell, and B. J. Eggleton, "Compact Brillouin devices through hybrid integration on silicon," *Optica*, vol. 4, no. 8, p. 847, Aug. 2017.

[35] R. Botter, K. Ye, Y. Klaver, R. Suryadharma, O. Daulay, G. Liu, J. Van Den Hoogen, L. Kanger, P. Van Der Slot, E. Klein, M. Hoekman, C. Roeloffzen, Y. Liu, and D. Marpaung, "Guided-acoustic stimulated Brillouin scattering in silicon nitride photonic circuits," *Science Advances*, vol. 8, no. 40, p. eabq2196, Oct. 2022.